Comparing Downburst and Tornado Signatures in Mesoscale Convective Systems between NEXRAD and Phased Array Radar

SEAN PHIPPS*

National Weather Center Research Experiences for Undergraduates Program
Norman, Oklahoma
Northern Illinois University
DeKalb, Illinois

KRISTOFER S. TUFTEDAL

NOAA National Severe Storms Laboratory
Cooperative Institute for Severe and High-Impact Weather Research and Operations
University of Oklahoma
Norman, Oklahoma

CHARLES M. KUSTER

NOAA/OAR National Severe Storms Laboratory
Norman, Oklahoma

VIVEK N. MAHALE

NOAA National Weather Service
Norman, Oklahoma

ABSTRACT

Dual-polarization (dual-pol) phased array radar (PAR) is being considered as a potential replacement to the current Weather Surveillance Radar-1988 Doppler (WSR-88D) network (NEXRAD) because of its high cost-benefits, better polarimetric data quality, and finer temporal resolution. Research on the utility of using dual-pol PAR to identify downburst signatures in mesoscale convective systems (MCSs) is limited; therefore, this study uses KTLX and KOUN NEXRAD radars and the National Severe Storms Laboratory's (NSSL's) Advanced Technology Demonstrator (ATD) S-band dual-pol PAR to compare temporal evolutions of specific differential phase (K_{DP}) core maxima in seven cores. Sampled K_{DP} cores are obtained from three MCSs; a warm season mesoscale convective complex (MCC) transition into a bow echo, a warm season bow echo, and a cold season quasi-linear convective system (QLCS). The QLCS case provided mesovortices for further analysis, in which this study uses quantifications of downdraft and circulation strength with ATD to identify correlations between storm characteristics. This analysis revealed that: 1) the K_{DP} genesis threshold was met earlier in ATD in all cases where it was measured; 2) K_{DP} and mesovortex sampling is incomplete with WSR-88D and sometimes misses transient K_{DP} cores; 3) one downburst indicated by a K_{DP} core and subsequent collapse augmented mesovortexgenesis in a cold-season QLCS case. These results support the conclusion that PAR enables the earlier detection of downburst precursor signatures and illuminates details of K_{DP} cores, collapses, and columns not captured by the current WSR-88D network.

1. Introduction

MCSs are organized groups of updrafts (where warm, moist air rises and condenses into clouds) and downdrafts (which bring evaporatively cooled air to the surface) and severe weather hazards such as damaging winds, flood-ing, tornadoes, and small hail are all common with MCSs. The primary difference compared to single cells is that MCSs promote internal interactions by propagating, merging, or interfering with other circulations within the system (Schumacher and Rasmussen 2020). Thus, the dynamics involved in each system largely depends on the morphology of the MCS, whether the system is a squall line (i.e. QLCS), bow echo, or MCC. As one example,

---

Corresponding author address: Sean Phipps, Northern Illinois University, 231 N Annie Glidden Rd, DeKalb, IL
E-mail: phippss0316@gmail.com

squall line longevity relies on a balance between environmental shear and negative vorticity generated by the cold pool (Rotunno et al. 1988; Coniglio and Stensrud 2001). Due to these factors, MCSs are challenging for radar analysis as there might be overlapping updrafts and downdrafts that 'wash out' signatures and MCSs come in diverse shapes and sizes that may prevent generalizations with precursor signatures.

Meteorologists have used radar networks to detect hydrometeors since the advent of the first Weather Surveillance Radars (WSRs) in the 1940s and 50s (Whiton et al. 1998). Since then, technologies such as doppler (i.e. WSR-1988 Doppler, WSR-88D) and dual-polarization (i.e., "dual-pol") have allowed researchers to remotely observe additional hydrometeor characteristics, such as the velocities and shape of particles. Novel radar scanning strategies, such as Automated Volume Scan Evaluation and Termination (AVSET) or Supplemental Adaptive Intra-Volume Low-Level Scans (SAILS), reduce scan times (Chrisman 2013, 2014). Both single and dual-pol products are used to connect radar data to conceptual models, detect what signatures are occurring at the time of the scan, and forecast perils that may manifest at the surface. Dual-polarization products are especially useful as they can observe scatterers in both horizontal and vertical "cross-sectional" perspectives, gaining additional insight on real-time microphysical processes occurring within a storm (Kumjian 2013b).

Prior to the operationalization of dual-pol, the main downburst precursor signature was a localized area of elevated Z_H called a reflectivity core (Peterson 1984; Roberts and Wilson 1989), along with an area of midlevel convergence observed in V_R called the mid-altitude radial convergence (MARC) signature. However, since Z_H has ambiguity with respect to precipitation type (Kumjian 2013a) and MARCs are not always discernible, studies have analyzed a supplemental signature called specific differential phase (K_{DP}) cores (Jung et al. 2012; Kuster et al. 2021). K_{DP} is preferred to forecast downbursts because of the dominance that melting hailstones have on elevating K_{DP} values (Kumjian et al. 2019). Recent research has correlated the existence of mid- and low- level K_{DP} cores to mesovortexgenesis (Kuster et al. 2024). Along with this, K_{DP} collapses can be used to identify areas of greater risk for downbursts (Frugis 2020); however, vertical translations in K_{DP} maxima are not holistically captured by NEXRAD and require finer temporal resolutions to better analyze these more transient signatures.

Phased Array Radar (PAR) is being considered as a replacement for the current NEXRAD network due to its faster update times and better polarimetric data quality, though the latter is not exclusively a PAR feature (Kollias et al. 2022). PAR takes advantage of electromagnetic properties to create a main lobe of maximum constructive interference from thousands of antennas, steered by changing the phase difference between the antennas. Because of this digital steering, PAR only takes one minute for a volumetric scan compared to the five of WSR-88D using volumetric coverage pattern (VCP) 212 (Palmer et al. 2022). Case studies that have used PAR notice advantages in depictions of short-term changes in signatures, such as rapid intensification and cycles of low and mid-level mesocyclones (Heinselman et al. 2008; Kuster et al. 2015) and descents of reflectivity cores (Kuster et al. 2016). As some examples, Heinselman et al. (2008) found that PAR demonstrated superior ability over the WSR-88D to identify signatures that indicate dynamical processes such as the MARC and low-altitude divergence. Kuster et al. (2016) also found that PAR is superior in identifying quickly-evolving downburst signatures, focusing on K_{DP} collapses and association with downburst intensification. NWS forecasters participating in a real-time warning experiment for hail and wind revealed that PAR has the potential to increase lead times, mastery, and confidence amongst participants (Bowden et al. 2015). Research WSR-88Ds have the ability to change their update times using adaptive scanning strategies and studies that have used these radars show similar results (Tanamachi and Heinselman 2016).

This study will focus on K_{DP} cores, subsequent descent, and transient mesovortexgenesis, all of which develop on small timescales that are hypothesized to be more holistically captured by PAR. We will be comparing WSR-88D data to PAR data by recording K_{DP} maxima through the domain of the core at all elevation angles. We will also analyze a time series of mesovortex and downburst characteristics to quantify influences between the two processes. Do notable differences exist between WSR-88D and PAR data? How long before mesovortex formation did K_{DP} cores begin to descend? Can we obtain more information about existing signatures using rapid-update data? Using this analysis, we can visualize and quantify the contrasts between WSR-88D and PAR, connect them to an operational perspective, and contribute to the knowledge on how much our forecasters could benefit from these data during "nowcasting" timescales.

2. Methods

a. Case and Radar Selection

To analyze the contrasts of small-scale signatures in MCSs with PAR and WSR-88D, cases were selected based on a given storm's proximity to the PAR site, data availability, morphology of the storm, and wind reports. We used PAR data from NSSL's ATD radar located in Max Westheimer airport (35° 14' 9.6" N, 97° 27' 46.8" W) in Norman, Oklahoma, collocated with the KOUN research radar. KTLX (35° 19' 58.8" N, 97° 16' 40.8" W) is located to the northeast if the data for KOUN is not available. Despite being located approximately 13 miles away,

this discrepancy was not expected to significantly affect comparisons between ATD and KTLX using our analysis technique. All radars used in our analysis operate at S-band, therefore comparisons between sites with respect to scattering regimes and KDP response are valid. However, there are slight differences with both vertical and horizontal resolution, given that the radars sometimes run on different VCPs and the PAR has differing azimuthal resolutions depending on the distance from the center radial of the 90-degree viewing sector.

To be considered for this study, a given MCS must have been within 120 km to ATD and KOUN/KTLX and within ATD's 90-degree viewing sector. Visual analysis was performed using the Warning Decision Support System-Integration Information (WDSS-II; Lakshmanan et al. 2007) to interrogate both PAR and WSR-88D data. We also wanted to compare radar observations to live storm reports, so we used data from the NCEI Storm Report Archive due to the strict quality control measures. However, at the time of writing, data from April 2024 onwards was not included as part of the archive. As such, the Storm Prediction Center (SPC) filtered storm reports were used for the analysis of any event past April 2024.

b. K_{DP} Core Analysis

When we began analysis of each case, we first identified the melting layer height. K_{DP} cores are primarily made up of melting hailstones that begin melting as they pass through the melting layer, thus cooling the air and adding to the negatively buoyant air inherent to downdrafts. For this study, we manually analyzed radar-based melting layer signatures to identify the height of the top and bottom of the layer. The top of the melting layer is determined by the height of the down-radial border of low cross-correlation coefficient (ρ_{HV}) and the bottom of the layer is the height of the up-radial border. To help identify potential candidates for analysis, we made an algorithm that uses the melting layer derived from soundings to determine the maximum K_{DP} value in or within 2 km of the melting layer. K_{DP} cores associated with wind or tornado reports were prioritized, though two null cases were included due to extreme K_{DP} values in those events.

After we identified candidate events, we tracked K_{DP} back in time until we found K_{DP} core genesis or had at least ten minutes of data. K_{DP} core measurements were restricted under an arbitrary spatial domain, acting as boundaries for the K_{DP} core. This spatial domain must primarily consist of $K_{DP} \geq 3\,^{\circ}\,km^{-1}$ with decreasing K_{DP} values approaching the boundaries of the domain. The $\geq 3\,^{\circ}\,km^{-1}$ K_{DP} threshold differs from precedent criteria such as $\geq 1\,^{\circ}\,km^{-1}$ (Kuster et al. 2021) because it is difficult to identify K_{DP} core genesis with the $1\,^{\circ}\,km^{-1}$ threshold due to the small signal-to-noise ratio at this value. We measured the time, site, height, and value of each K_{DP}

maxima to illuminate temporal trends, comparing them to mesovortexgenesis and tornado report times. A total of four K_{DP} events in three MCS cases were studied: a warm season MCC transition into a bow echo (2 May 2024), a warm season bow echo (23 June 2023), and a cold season QLCS (27 February 2023). Additionally, to understand the larger-scale environment influencing each case, we used the SPC Mesoanalysis archive to analyze environmental conditions and synoptic forcing mechanisms.

c. Mesovortex Analysis

To quantify the possible augmentation of mesovortices due to downbursts, we use precedent criteria to define a mesovortex: a rotational velocity (V_{rot}) of at least $10\,m\,s^{-1}$ (19.4 kts) extending to a depth of at least 2.4 km for two scans or more (Thompson et al. 2012; Kuster et al. 2024). V_{rot} is calculated using (1)

$$v_{rot} = \frac{v_{in} - v_{out}}{2} \qquad (1)$$

where V_{out} and V_{in} are the maximum outbound and inbound V_Rs within a velocity couplet, respectively.

Since other studies used non-rapid-update data, we reduced the temporal continuity threshold from five minutes on WSR-88D data to one minute for PAR data. We allowed for more transient mesovortices due to the lower temporal continuity threshold, so results pertaining to precursor signatures may not reflect mesovortices that impact the surface. If the signature had an associated tornado or wind report, we noted the strength with the Enhanced Fujita (EF) Scale or knots, respectively.

Because we are measuring transient mesovortices that may not manifest at the surface, it is useful to quantitatively measure local maxima of cyclonic shear. This study uses two methods: V_{rot}, as specified previously in (1), and an azimuthal shear (AzShear; Mahalik et al. 2019) algorithm. Rather than taking one measurement for the shear gradient, AzShear uses the linear least squares derivative technique, which takes multiple gradients over a domain called a kernel. The kernel can be adapted to many sizes depending on its purpose, but an azimuthal kernel width of 2.5 km is most accurate for tornado identification. Similarly, since we want to view the downburst's influence on mesovortices, we quantify surface divergence using divergent shear (DivShear; Mahalik et al. 2019), which uses a similar method as AzShear, but takes the radial derivative as opposed to the azimuthal derivative. Measurements of AzShear and DivShear maxima used arbitrary domains centered over the V_R couplet and divergence center, respectively. To determine bounds for the AzShear domain, we used a hard threshold of one adjacent AzShear gate on each side of the gate collocated with the V_R couplet. For the domain bounds of DivShear, we used the size of the radial divergence signature (i.e., V_{in}/V_{out} values next to
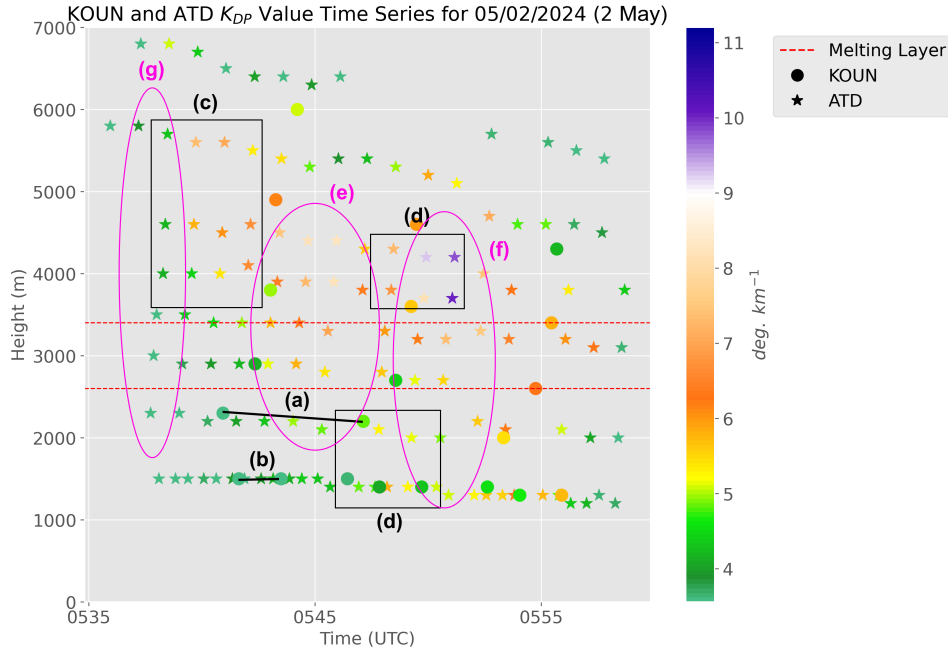
FIG. 1. Time series of maximum K_{DP} value (colors) with respect to height (meters) from 053527 to 055841 UTC on 2 June 2024. Star (circle) shaped markers denote K_{DP} values from ATD (KOUN). The melting layer is enclosed within the two dashed red lines. The annotations represent the following: (a) and (b), an example of a volumetric and SAILS scan time respectively for KTLX; (c) and (d), sudden increases in K_{DP}; (e) and (f), vertically discontinuous K_{DP} columns; (g), vertically continuous K_{DP} column.

each other along a given radial). We also record maximum V_R for both the downburst and mesovortex in each scan to approximate the magnitude of the wind field, though this has significant limitations based on the orientation of the storm with respect to the radar because V_R only measures the radial component of velocity.

3. Results

a. 2 May 2024

For 2 May, there was little synoptic forcing due to the meager upper-level flow and lack of frontal features. Around the timeframe of Figure 1 (0500 UTC), surface-based convective available potential energy (SBCAPE) decreased to around 2000 $J \ kg^{-1}$ while surface-based convective inhibition (SBCIN) increased due to diurnal cooling. Mixed-layer CAPE (MLCAPE) shows similar values of around 1500 $J \ kg^{-1}$. Downdraft CAPE (DCAPE) was over 1100 $J \ kg^{-1}$ in central Oklahoma because of dry air at 700 hPa and modest dew point depressions at the surface. In terms of shear, effective bulk shear was less than 30 kts because of weak upper-level flow. However, 0-1 km storm relative helicity (01SRH) was over 150 $m^2 s^2$ and low-level storm-relative winds were over 25 kts in response to the low-level jet (LLJ). Precipitable water (PWAT) is also an influence of melting hailstone generation (Kumjian et al. 2019), the value in this case was around 1.3 inches.

Figure 1 shows a time series of K_{DP} core maxima $\geq 3 \circ km^{-1}$ for all tilts. Some features are universal amongst all four K_{DP} events, most notably the amount of volume scans each radar completes. Temporal resolutions of scans aloft and those associated with SAILS are finer in ATD than KOUN. On average, ATD is able to complete five volumes for every one WSR-88D volume (5:1 ratio, Fig. 1a) with SAILS ratios varying between 2:1–4:1 (e.g. Fig. 1b). Using our definition of a K_{DP} core (Section 2), the ATD first detects a K_{DP} core 3 minutes and 12 seconds before KOUN. In the 25 minutes between 053527 and 055841 UTC, the ATD sampled K_{DP} cores between 1.2–6.8 km 126 times while KOUN only sampled K_{DP} cores 21 times (Fig. 1). There are many examples of K_{DP} values sharply increasing in the ATD data, such as 0539–0543 UTC above the (Fig. 1c) and 0548–0549 UTC both above and below the melting layer (Fig. 1d). There are also examples of sharp vertical gradients, such as 0538–0547 UTC (Fig. 1e) and 0548–0551 UTC (Fig. 1f) around the melting layer. We classify these K_{DP} columns as "vertically discontinuous," as there are higher values of K_{DP} above the melting layer than those within or below the melting layer. An example of a vertically continuous column would be the first volume scan on 2 May (Fig. 1g), indicating mostly uniform K_{DP} values throughout both layers. No wind or tornado reports were associated with these K_{DP} signatures.
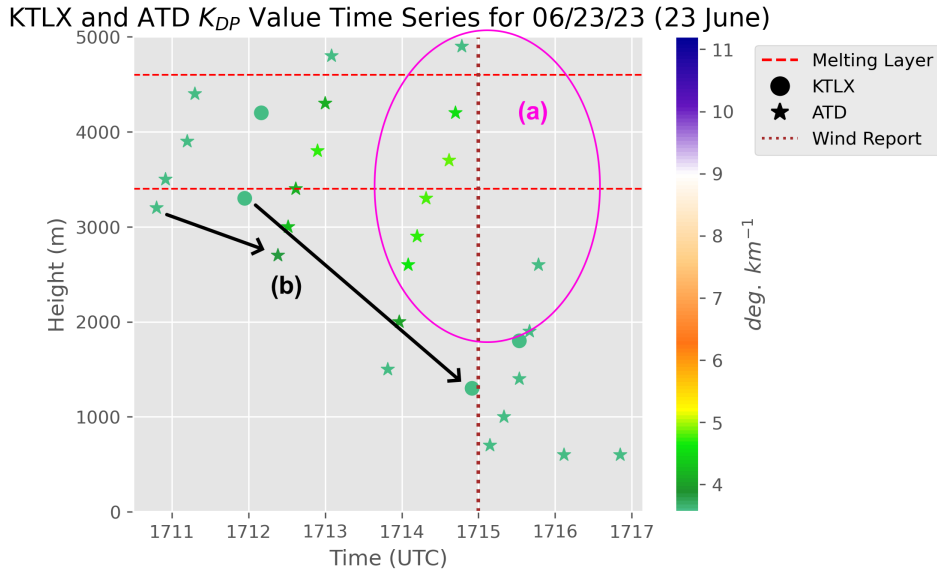
FIG. 2. As in Fig. 1, but from 171048 to 171651 UTC on 23 June 2023 and circles now represent KTLX instead of KOUN. The brown dashed line indicates the time of a wind report. The annotations represent the following: (a), vertically continuous K_{DP} column reduction under the K_{DP} core threshold; (b), K_{DP} core descent captured by ATD and KTLX in order.

b. 23 June 2023

23 June was another case where synoptic forcing was nebulous with just 35 kts of 500 hPa flow and no obvious surface boundaries. At 1700 UTC, SBCAPE reached around 2500 $J\ kg^{-1}$ with less than 2000 $J\ kg^{-1}$ of ML-CAPE. Substantial erosion of SBCIN before 1700 UTC complemented the initiation of this complex. For this event, meager DCAPE on the order of 800 $J\ kg^{-1}$ was associated with low dew point depressions near the surface. Effective bulk shear was quite low, at less than 30 kts, same as 2 May. However, 01SRH is less (50 $m^2 s^2$) than 2 May because of the lack of an LLJ response at this time of day. PWAT was also much higher than 2 May with values ranging between 1.7–2 inches.

K_{DP} did not reach magnitudes on 23 June as large as those shown on 2 May (Figure 2). K_{DP} maxima measured by ATD reaches the $\geq 3\ ^{\circ}\ km^{-1}$ threshold 1 minute and 9 seconds sooner than KTLX. In the six minutes between 171048 and 171651 UTC, the ATD sampled K_{DP} cores between 0.6–4.9 km 25 times while KTLX only sampled K_{DP} values four times (Fig. 2). Spatially, this K_{DP} core was primarily located near the downshear tip of the rear inflow jet (RIJ, Fig. 3). Vertically continuous K_{DP} columns are identified up until the wind report at 1715 UTC, then the column signature reduces under the threshold (Fig. 2a). The wind report is correlated with $\geq 3\ ^{\circ}\ km^{-1}$ values at 700 m on ATD soon after 1715. We also notice that ATD data sampled descent of the K_{DP} core earlier than KTLX did (Fig. 2b).

c. 27 February 2023

27 February is different from the previous two cases in morphology, environment, and most notably synoptic forcing. A 500 hPa trough was present and a surface low deepened to 990 hPa in western Kansas by 0300 UTC. A QLCS developed along the cyclone's associated cold front. SBCAPE during this time was only at 250 $J\ kg^{-1}$, with MLCAPE a bit larger at around 750 $J\ kg^{-1}$. Both SBCIN and MLCIN have large values greater than 100 $J\ kg^{-1}$, though this is compensated for by the amount of forcing for ascent. This is the only case that has a high effective bulk shear, with 70–80 kts in southwest Oklahoma by 0200–0300 UTC. These values are extreme because of the 500 hPa trough enhancing upper-level flow along with the surface response of the anticyclone and LLJ. Analogously, 01SRH is also at extreme values with 800 $m^2 s^2$. PWAT is the lowest out of all three cases with 1.1 inches.

In the 27 minutes between 023332–030142 UTC, the ATD sampled the K_{DP} core 141 times while KTLX sampled K_{DP} cores between 0.3–5.5 km 38 times. Temporal resolution ratios varied from 3:1–4:1 aloft to 2:1–3:1 at the 0.5-degree elevation angle with SAILS scans (not shown). For this case, we did not record when either radar first reached the K_{DP} threshold, though ATD detected sharp increases in K_{DP} (e.g. 0234, 0240, 0253) sooner than KTLX with varying magnitudes (Fig. 4a). One time in particular (0253 UTC) occurred between two consecutive KTLX volume scans (Fig. 4b), though this is a different evolution compared to 0.5-degree SAILS tilt that shows an increasing K_{DP} core around 0255 UTC. We identify both
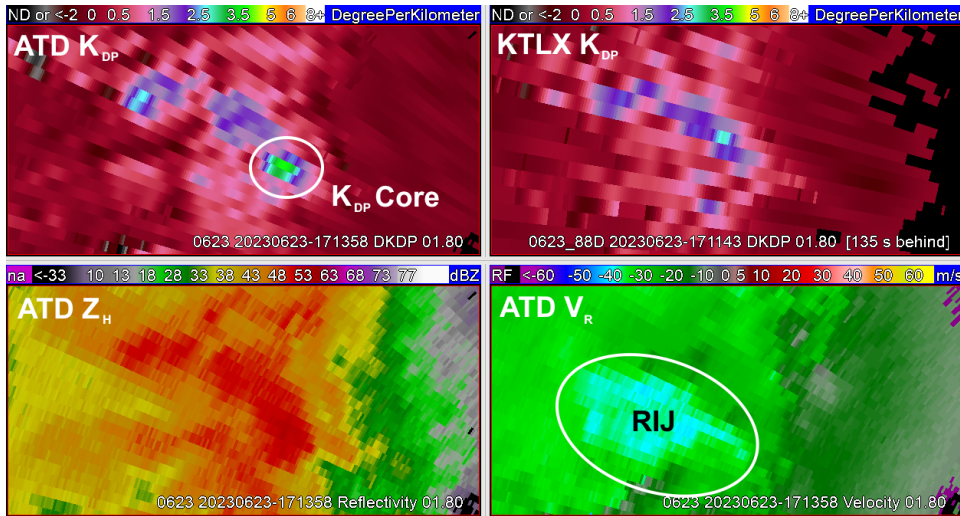
FIG. 3. Planned position indicator (PPI) scan of ATD K_{DP} (top-left), KTLX K_{DP} (top-right), ATD horizontal reflectivity (bottom-left), and ATD V_R (bottom-right) on 23 June 2023. ATD scans occurred at 171358 while the KTLX scan occurred at 171143, 135 seconds behind ATD. The K_{DP} core and RIJ are circled and labeled.
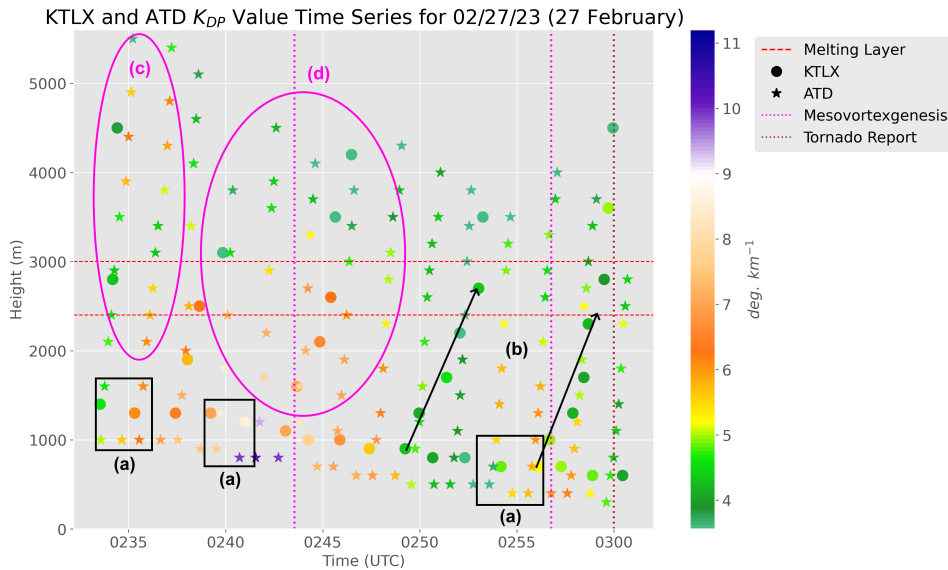

FIG. 4. As in Fig. 2, but from 023332 to 030042 UTC on 27 February 2023 Pink dashed lines represent mesovortexgenesis and the brown dashed line indicates a tornado report. The annotations represent the following: (a), sharp increases in K_{DP}; (b), KTLX volume scans missing one increase in K_{DP} displayed in (a); (c), vertically discontinuous K_{DP} column; (d), vertically continuous K_{DP} column that persists for the rest of this timeseries.

vertically discontinuous (0233–0236 UTC, Fig. 4c) and continuous (0236 UTC onwards, Fig. 4d) K_{DP} columns throughout the timeframe of Figure 4. Two V_R signatures met the criteria for mesovortices in this analysis, and K_{DP} values elevate to $9° km^{-1}$ at 800 m (0240 UTC) before the first mesovortex develops. The K_{DP} maxima at 024333 UTC was collocated with V_R divergence and a mesovortex to its north (Figure 5). The second mesovortex (0257 UTC) was associated with an EF0 tornado report but was

located much further north of the V_R divergence and 0.5-degree K_{DP} core (Figure 6).

Figure 7 begins shortly after 0300 UTC on 27 February and is located at a different region of the QLCS. In the 10 minutes between 030015–031032 UTC, The ATD sampled the K_{DP} cores 84 times between 0.2–3.8 km, while KTLX sampled the K_{DP} cores 15 times. A sharp increase in K_{DP} aloft occurs at 0304 UTC (Fig. 7a) and then closer to the surface shortly after at 0305 UTC (Fig. 7b), in-
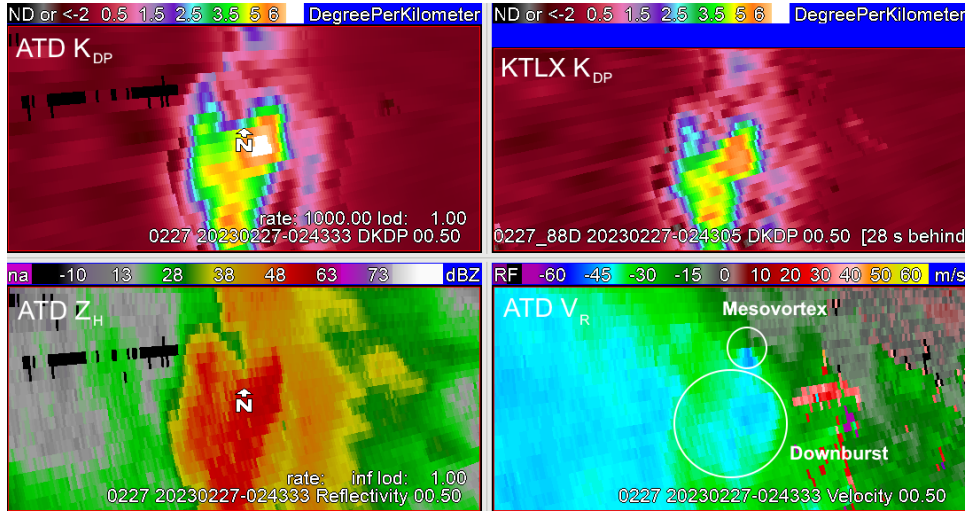
FIG. 5. As in Fig. 3, but on 27 February 2023 with the downburst and mesovortex circled and labeled. ATD scans occurred at 024333 while the KTLX scan occurred at 024305, 28 seconds behind ATD.
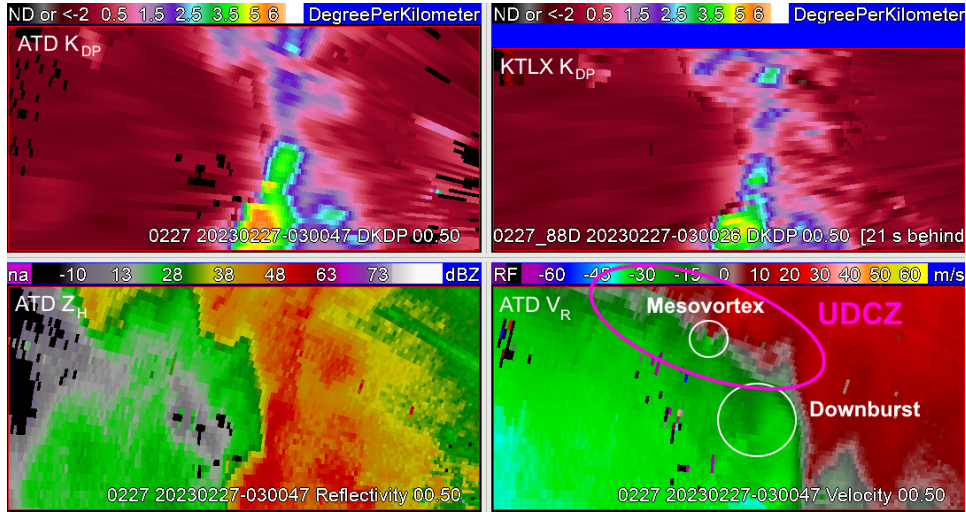

FIG. 6. As in Fig. 5, but at 030047 for ATD and 030026 for KTLX. KTLX is 21 seconds behind ATD. The pink circle is for the updraft-downdraft convergence zone (UDCZ).

dicating a K_{DP} collapse. This collapse was associated with a strong divergent V_R response where DivShear values reached 0.00754 s^{-1}. All K_{DP} column signatures in 27 February-Null are vertically continuous besides the first ATD volumetric scan displaying discontinuity in the melting layer (Fig. 7c).

Figure 8 displays a time series of downburst and mesovortex maxima at the 0.5-degree tilt (0.5–1 km ARL) from 023639 to 024934 UTC. When the K_{DP} core reaches its maximum value at the lowest tilt just after 0240 UTC, there is an increase in DivShear from 0.00161 s^{-1} to 0.00294 s^{-1}, the most significant jump in this time series. This jump in DivShear occurs at the same time as mesovortex inbound velocity, V_{rot}, and AzShear jumps (Fig. 8a); however, other significant jumps in the mesovortex characteristics were not correlated to a DivShear increase (Fig. 8b). Trends of rotational velocity and AzShear correlate until 0245, where they begin to diverge as V_{rot} decreases while AzShear maintains its value (Fig. 8c). We suspect that this discrepancy exists because a) the mesovortex is near a strong UDCZ (Fig. 5) and, since AzShear takes the azimuthal gradient over a domain, the total shear over the area may not be mesovortex dominant; and/or b) the diameter of the mesovortex is decreasing (not shown) while V_{rot} also decreases (Fig. 8c). The V_{rot} maximum also occurs 1 minute and 10 seconds after the mesovortex and downburst inbound peak V_Rs are reached.
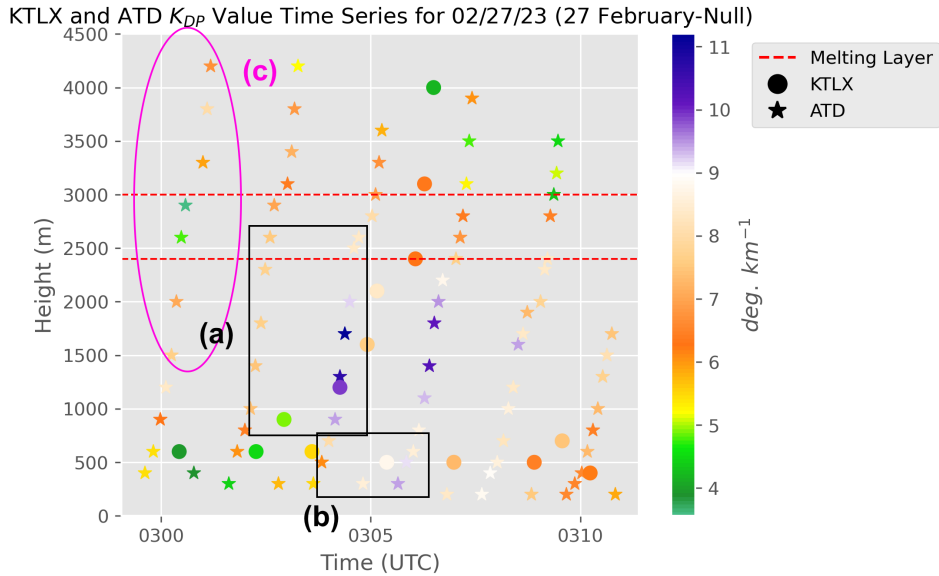
FIG. 7. As in Fig. 2, but from 030015 UTC to 031032 UTC on 27 February 2023. The annotations represent the following: (a), sharp increase in K_{DP} over time below the melting layer; (b), sharp increase in K_{DP} less than 750 m. Since this increase occurred after and below (a), we consider this a collapse; (c), vertically discontinuous K_{DP} column.
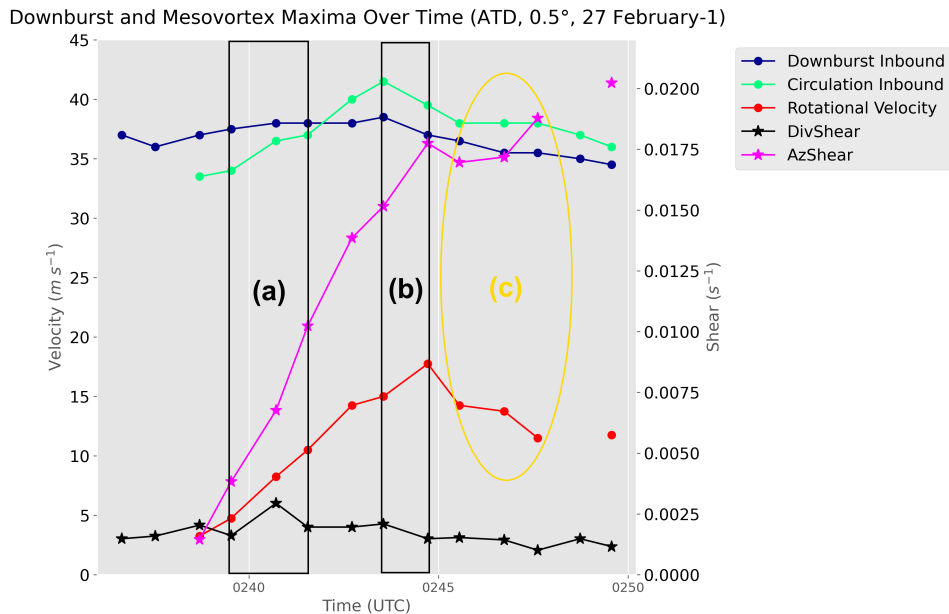

FIG. 8. Time series comparison of various ATD mesovortex and downburst quantifications of the first mesovortex on 27 February 2023. Samples taken at the 0.5-degree elevation angle (0.5 km to 1 km ARL) from 023639 to 024934 UTC. Characteristics with circle (star) markers match the velocity (shear) y-axis. The green, red, and pink lines are associated with mesovortex characteristics while the black and navy blue lines are associated with downburst characteristics. The annotations represent the following: (a) increase in DivShear correlating to increases in mesovortex strength; (b) increase in mesovortex quantifications not correlated with a DivShear increase; (c) divergence of AzShear and rotational velocity values, different from the correlations earlier in the time series.

Figure 9 displays the same characteristics as Fig. 8, but from 024844 to 030338 UTC and at a different position in the QLCS. Figure 9a clearly displays the limitations of us-

ing V_R to analyze mesovortex and downburst interactions. At this time, the K_{DP} core was located to the NNW of ATD moving nearly due east, radial components of Earth-
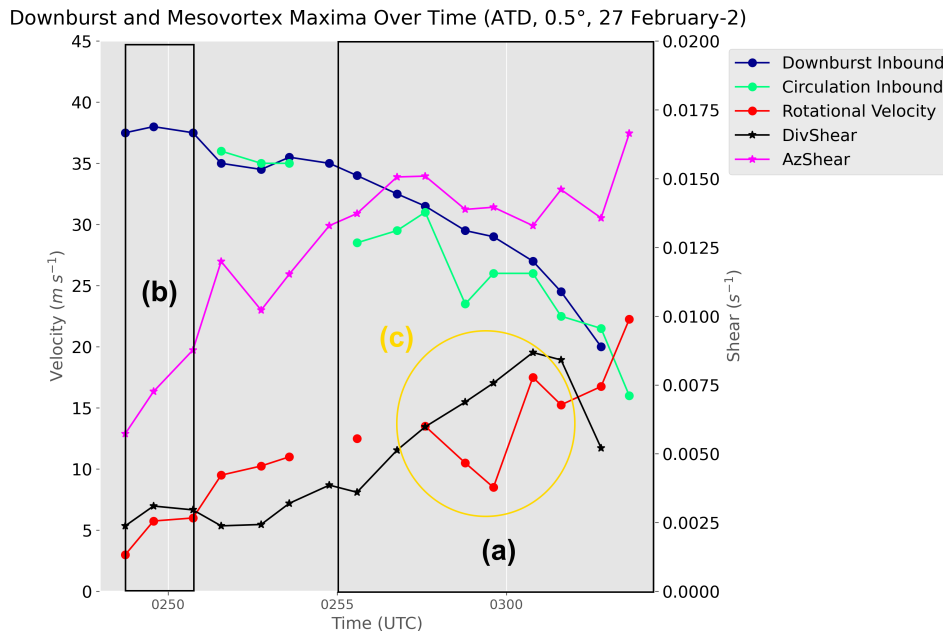
FIG. 9. As in Fig. 8, but from 024844 to 030338 UTC on 27 February 2023 measuring mesovortex two of the K_{DP} event. The annotations represent the following: a) storm orientation biases with quantifications measuring V_R; b) positive correlations between downburst and mesovortex quantifications associated with a circulation that did not meet the mesovortex threshold; c) substantial yet transient fluctuation in rotational velocity.

relative wind measurements rapidly decreased. This limitation also applies to DivShear as along-azimuth gradients in quasi-linear features are a function of a given feature's orientation to the radar (i.e., it is maximized when the V_R gradient is perpendicular to the radar beam), but did not apply to V_{rot} or AzShear since the signatures they are measuring are circular (Mahalik et al. 2019). Nonetheless, we identify an increase of DivShear towards the beginning of data collection that is collocated with a meager circulation, but did not meet the criteria of a mesovortex (Fig. 9b, circulation not shown). We see both V_{rot} and AzShear increasing, along with fluctuations throughout the lifespan of the circulation. In the largest fluctuation, V_{rot} decreases substantially from 13.5 $m\ s^{-1}$ to 8.5 $m\ s^{-1}$ and back up to 17.5 $m\ s^{-1}$ in three minutes (Fig. 9c). Notice that V_{rot} fluctuates above and below the mesovortex threshold in less time than an average WSR-88D volume scan (5 minutes), but a little more time than a typical SAILS scan (2.5 minutes) on a WSR-88D.

4. Discussion

a. Meeting Thresholds and the Warning Process

In the time series where we began data analysis of K_{DP} core generation, ATD met the K_{DP} threshold of 3 $^\circ km^{-1}$ below the melting layer minutes before the WSR-88D regardless of if the radar was collocated or not. This does not necessarily mean that, in a real forecasting scenario, a downburst precursor signature would be identified sooner

on a PAR than a WSR-88D since NWS forecasters generally look at trends in the data when making a warning determination. However, Bowden et al. (2015) suggests that PAR enables more mastery (i.e., confident and correct) decisions and longer lead times in severe wind and hail events. We suggest this result is because of the rapid-update scans above the 0.5-degree level, shown by the larger ratios (3:1–5:1) of scans aloft than SAILS ratios (2:1–3:1). This is particularly applicable to K_{DP} cores since they usually form near the melting layer. Unless the WSR-88D is at range where the base scan reaches these levels (which would further muddy the signature due to range degradation), K_{DP} core developments aloft only have one opportunity to be detected every 5+ minutes using the rapidly evolving severe weather standard VCP 212. This analysis does not account for other downburst precursor signatures that may develop over a longer time.

b. Incomplete Picture of K_{DP} Core Developments, Collapses, and Mesovortices

In all cases with K_{DP} core collapses, WSR-88D data were shown to either underrepresent (23 June, 2 May, 27 February-Null) or completely miss (27 February) these signatures compared to the ATD. For the latter case, the WSR-88D could not resolve the second K_{DP} core because it developed and dissipated between volume scans. This transient K_{DP} collapse does influence the V_R field, so it can be assumed that such cores have the possibility to affect

the complex dynamical processes of MCSs and highlights the need to have rapid-update radar observations of these features. 2 May and 27 February-Null had K_{DP} cores and core collapses that were captured by both ATD and WSR-88D radars; however, quicker sampling of hydrometeors aloft from ATD allowed for gradual changes in the K_{DP} core characteristics below the melting layer to be seen in both cases. These changes could help increase forecaster confidence in an imminent K_{DP} core collapse before it is observed near the surface.

c. K_{DP} Cores Preceedng Mesovortexgenesis

27 February displayed two downburst signatures that preceded mesovortexgenesis, but the downburst signature, and associated K_{DP} core collapse, was much closer in proximity to the mesovortex compared to the second. Therefore, it can be inferred that the K_{DP} core collapse and resulting downburst affected mesovortex generation in some capacity. However, determining what effect K_{DP} core collapse has on mesovortex generation is less clear because of it being seen in a single case. We hypothesize that downbursts can act as a pseudo-rear flank downdraft surge, similar to how a descending RIJ can lead to mesovortexgenesis by increasing local vorticity at the surface (Wheatley and Trapp 2008; Atkins and St. Laurent 2009; Flournoy and Coniglio 2019). Quantifying relationships between downburst and mesovortex characteristics in Figure 8 revealed that a jump in DivShear that correlated with the K_{DP} collapse seemed to also correlate with jumps in inbound V_R, V_{rot}, and AzShear. However, other jumps in the latter three characteristics display similar magnitudes but no DivShear correlation, implying that there are other processes involved in the genesis and maintenance of the mesovortex.

5. Conclusion

In this study, we compared downburst signatures in three distinct MCSs between dual-pol PAR and WSR-88D and analyzed quantifications of collocated circulations and downbursts using PAR. Depending on data availability, we compared either NSSL's ATD to KTLX or KOUN and used tornado or wind reports from the SPC or NCEI database to aid in analysis. For radar data, KOUN is collocated with ATD but is limited in number of cases. For reports, NCEI has better quality checking but does not have 2024 data. We plotted K_{DP} maxima throughout the K_{DP} cores under the restriction of an arbitrary domain that was representative of the K_{DP} core size. Then, we related these K_{DP} maxima to mesovortexgenesis, wind reports, and tornado reports. In further mesovortex analysis, we used ATD to compare quantifiable trends in both downbursts and mesovortices. We used DivShear and V_R to quantify downburst strength and we used AzShear, rotational velocity, and V_R to quantify mesovortex strength.

Time series analysis with four K_{DP} events in three MCS cases support the following conclusions:

- In cases where we captured the genesis of K_{DP} cores below the melting layer, ATD met the $3\ ^{\circ}\ km^{-1}$ threshold earlier than both KTLX and KOUN in all cases. However, this does not necessarily mean that lead times would increase as forecasters generally look at trends when determining precursor signatures. We suggest that the amount of information gained aloft can decrease the amount of time it takes to determine that a K_{DP} core is present.

- K_{DP} sampling aloft is incomplete using existing WSR-88D VCPs. Both KOUN and KTLX missed sudden K_{DP} increases and transient K_{DP} core development. WSR-88D radars also missed fluctuations in mesovortex characteristics. Since forecasters rely on trends to make signature determinations, a sudden increase in K_{DP} aloft acts as a "flag" and thus could affect the warning process.

- In one cold-season QLCS case, we identified one K_{DP} collapse and associated downburst that probably augmented mesovortexgenesis through increased convergence and subsequent enhanced stretching of low-level vorticity. Although it is unclear in what ways the downburst affected mesovortex evolution, the results from this case are supported by the results in Kuster et al. (2024).

This study supported previous research pertaining to faster and more reliable detection of downburst precursor signatures. Additionally, we contributed to the ongoing investigation of downburst signature manifestation and downburst augmentation of mesovortices by comparing WSR-88D and PAR data. Future work should assess a larger sample size of K_{DP} cores to analyze relationships (spatial, temporal, morphological, etc.) between downburst signatures that produce damaging winds in MCSs and those that do not. Future research should also evaluate if and how both vertically continuous and discontinuous K_{DP} columns correlate to downburst intensity and perils.

References

Atkins, N. T., and M. St. Laurent, 2009: Bow echo mesovortices. part II: Their genesis. *Mon. Wea. Rev.*, **137 (5)**, 1514–1532, doi:10.1175/2008MWR2650.1.

Bowden, K. A., P. L. Heinselman, D. M. Kingfield, and R. P. Thomas, 2015: Impacts of phased-array radar data on forecaster performance during severe hail and wind events. *Wea. Forecasting*, **30 (2)**, 389–404, doi:10.1175/WAF-D-14-00101.1.

Chrisman, J. N., 2013: Dynamic scanning. *NEXRAD Now, No. 22*, 1–3, https://www.roc.noaa.gov/WSR88D/PublicDocs/NNOW/NNow22c.pdf.

Chrisman, J. N., 2014: The continuing evolution of dynamic scanning. *NEXRAD Now, No. 23*, 8–13, http://www.roc.noaa.gov/WSR88D/PublicDocs/NNOW/NNow23a.pdf.

Coniglio, M. C., and D. J. Stensrud, 2001: Simulation of a progressive derecho using composite initial conditions. *Mon. Wea. Rev.*, **129 (7)**, 1593–1616, doi:10.1175/1520-0493(2001)129⟨1593:SOAPDU⟩2.0.CO;2.

Flournoy, M. D., and M. C. Coniglio, 2019: Origins of vorticity in a simulated tornadic mesovortex observed during PECAN on 6 july 2015. *Mon. Wea. Rev.*, **147 (1)**, 107–134, doi:10.1175/MWR-D-18-0221.1.

Frugis, B. J., 2020: The use of collapsing specific differential phase columns to predict significant severe thunderstorm wind damage across the northeastern united states. Eastern Region Technical Attachment 2020-04, NOAA.

Heinselman, P. L., D. L. Priegnitz, K. L. Manross, T. M. Smith, and R. W. Adams, 2008: Rapid sampling of severe storms by the national weather radar testbed phased array radar. *Wea. Forecasting*, **23 (5)**, 808–824, doi:10.1175/2008WAF2007071.1.

Jung, Y., M. Xue, and M. Tong, 2012: Ensemble kalman filter analyses of the 29–30 may 2004 oklahoma tornadic thunderstorm using one- and two-moment bulk microphysics schemes, with verification against polarimetric radar data. *Mon. Wea. Rev.*, **140 (5)**, 1457–1475, doi:10.1175/MWR-D-11-00032.1.

Kollias, P., and Coauthors, 2022: Science applications of phased array radars. *Bull. Amer. Meteor. Soc.*, **103 (10)**, E2370–E2390, doi:10.1175/BAMS-D-21-0173.1.

Kumjian, M., 2013a: Principles and applications of dual-polarization weather radar. part i: Description of the polarimetric radar variables. *J. Oper. Meteor.*, **1 (19)**, 226–242, doi:10.15191/nwajom.2013.0119.

Kumjian, M., 2013b: Principles and applications of dual-polarization weather radar. part II: Warm- and cold-season applications. *J. Oper. Meteor.*, **1 (20)**, 243–264, doi:10.15191/nwajom.2013.0120.

Kumjian, M. R., Z. J. Lebo, and A. M. Ward, 2019: Storms producing large accumulations of small hail. *J. Appl. Meteor. Climatol.*, **58 (2)**, 341–364, doi:10.1175/JAMC-D-18-0073.1.

Kuster, C. M., B. R. Bowers, J. T. Carlin, T. J. Schuur, J. W. Brogden, R. Toomey, and A. Dean, 2021: Using KDP cores as a downburst precursor signature. *Wea. Forecasting*, **36 (4)**, 1183–1198, doi:10.1175/WAF-D-21-0005.1.

Kuster, C. M., P. L. Heinselman, and M. Austin, 2015: 31 may 2013 el reno tornadoes: Advantages of rapid-scan phased-array radar data from a warning forecaster's perspective*. *Wea. Forecasting*, **30 (4)**, 933–956, doi:10.1175/WAF-D-14-00142.1.

Kuster, C. M., P. L. Heinselman, and T. J. Schuur, 2016: Rapid-update radar observations of downbursts occurring within an intense multicell thunderstorm on 14 june 2011. *Wea. Forecasting*, **31 (3)**, 827–851, doi:10.1175/WAF-D-15-0081.1.

Kuster, C. M., K. D. Sherburn, V. N. Mahale, T. J. Schuur, O. F. McCauley, and J. S. Schaumann, 2024: Radar signatures associated with quasi-linear convective system mesovortices. *Wea. Forecasting*, doi:10.1175/WAF-D-23-0144.1.

Lakshmanan, V., T. Smith, G. Stumpf, and K. Hondl, 2007: The warning decision support system–integrated information. *Wea. Forecasting*, **22 (3)**, 596–612, doi:10.1175/WAF1009.1.

Mahalik, M. C., B. R. Smith, K. L. Elmore, D. M. Kingfield, K. L. Ortega, and T. M. Smith, 2019: Estimates of gradients in radar moments using a linear least squares derivative technique. *Wea. Forecasting*, **34 (2)**, 415–434, doi:10.1175/WAF-D-18-0095.1.

Palmer, R., and Coauthors, 2022: A primer on phased array radar technology for the atmospheric sciences. *Bull. Amer. Meteor. Soc.*, **103 (10)**, E2391–E2416, doi:10.1175/BAMS-D-21-0172.1.

Peterson, J., Robert E., 1984: A triple-doppler radar analysis of a discretely propagating multicell convective storm. *Journal of the Atmospheric Sciences*, **41 (20)**, 2973–2990, doi:10.1175/1520-0469(1984)041⟨2973:ATDRAO⟩2.0.CO;2.

Roberts, R. D., and J. W. Wilson, 1989: A proposed microburst nowcasting procedure using single-doppler radar. *J. Appl. Meteor. Climatol.*, **28 (4)**, 285 – 303, doi:10.1175/1520-0450(1989)028⟨0285:APMNPU⟩2.0.CO;2, place: Boston MA, USA Publisher: American Meteorological Society.

Rotunno, R., J. Klemp, and M. Weisman, 1988: A theory for strong, long-lived squall lines. *J. Atmos. Sci.*, **45**, 463–485, doi:10.1175/1520-0469(1988)045⟨0463:ATFSLL⟩2.0.CO;2.

Schumacher, R. S., and K. L. Rasmussen, 2020: The formation, character and changing nature of mesoscale convective systems. *Nat. Rev. Earth Environ.*, **1 (6)**, 300–314, doi:10.1038/s43017-020-0057-7.

Tanamachi, R. L., and P. L. Heinselman, 2016: Rapid-scan, polarimetric observations of central oklahoma severe storms on 31 may 2013. *Wea. Forecasting*, **31 (1)**, 19–42, doi:10.1175/WAF-D-15-0111.1.

Thompson, R. L., B. T. Smith, J. S. Grams, A. R. Dean, and C. Broyles, 2012: Convective modes for significant severe thunderstorms in the contiguous united states. part II: Supercell and QLCS tornado environments. *Wea. Forecasting*, **27 (5)**, 1136 – 1154, doi:10.1175/WAF-D-11-00116.1, place: Boston MA, USA Publisher: American Meteorological Society.

Wheatley, D. M., and R. J. Trapp, 2008: The effect of mesoscale heterogeneity on the genesis and structure of mesovortices within quasilinear convective systems. *Mon. Wea. Rev.*, **136 (11)**, 4220–4241, doi:10.1175/2008MWR2294.1.

Whiton, R. C., P. L. Smith, S. G. Bigler, K. E. Wilk, and A. C. Harbuck, 1998: History of operational use of weather radar by u.s. weather services. part i: The pre-NEXRAD era. *Wea. Forecasting*, **13 (2)**, 219–243, doi:10.1175/1520-0434(1998)013⟨0219:HOOUOW⟩2.0.CO;2.